Activating COOH* intermediate by Ni/Ni3ZnC0.7 heterostructure in porous N-doped carbon nanofibers for boosting CO2 electroreduction

Xinxin Wei [a,1], Shuhao Xiao [a,1], Rui Wu [a,*], Zhaozhao Zhu [a], Lei Zhao [a], Zhao Li [a], Junjie Wang [a], Jun Song Chen [a,*], Zidong Wei [b,*]

[a] School of Materials and Energy, University of Electronic Science and Technology of China, Chengdu 611731, PR China
[b] School of Chemistry and Chemical Engineering, Chongqing University, Chongqing 400044, PR China

ARTICLE INFO

ABSTRACT

Electrochemical reduction of CO_2 (CO_2RR) to value-added chemicals is a feasible strategy to build a carbon neutral society and store energy. However, the sluggish kinetics of CO_2RR accompanied by competing hydrogen evolution reaction (HER) makes the practical application of this process very challenging. Herein, we construct a $Ni/Ni_3ZnC_{0.7}$ heterostructured catalyst wrapped in porous N-doped carbon nanofibers via a facile electrospinning strategy for CO_2RR. Remarkably, the as-prepared $Ni/Ni_3ZnC_{0.7}$ catalyst exhibits a high selectivity of 91.5% toward CO, a superior CO partial current density of 11 mA cm^{-2} at −0.8 V versus the reversible hydrogen electrode (vs. RHE) and maintaining 93.4% of its initial selectivity after 45 h of continuous electrolysis. The calculation results of density functional theory (DFT) show that the heterostructure of $Ni/Ni_3ZnC_{0.7}$ catalyst is beneficial to the formation of *COOH and enhances the efficiency of electrocatalytic CO_2 conversion.

1. Introduction

Electrochemical reduction of CO_2 (CO_2RR) to value-added chemicals and fuel products (e.g., CO, CH_4, HCOOH, C_2H_4, etc.) has been considered as an effective strategy to realize a carbon neutral environment because it can be carried out under mild conditions, such as room temperature and ambient pressure [1–4]. However, due to the high stability of the C═O chemical bond of CO_2, it will lead to sluggish kinetics and high overpotential in CO_2RR, so high-performance electrocatalysts are urgently needed to enhance the efficiency of such an electrochemical process [5–8]. Although noble metals (e.g., Au, Ag and Pd) exhibited excellent performance during the CO_2-to-CO conversion process, the high cost and scarcity hampers their large-scale applications [9–12]. Therefore, it is of great significance to develop high-performance and non-precious alternatives to replace noble catalysts.

Recently, numerous studies have reported that non-precious metal Ni-based materials including nickel-nitrogen-carbon (Ni-N-C), single-atom, alloys and composites etc. can effectively catalyze the CO_2 electroreduction [13–16]. Among them, Ni-N-C has been widely recognized as one of the most promising catalysts for CO_2RR because of their high

activity, simple preparation and durable stability [17,18]. However, there are still remaining challenges to further boost the sluggish kinetics of proton-coupled electron transfer processes to meet the requirements for practical applications [19]. In order to boost the conduction of the charges during this electrochemical reaction, heterostructure engineering is one of the effective strategies, where interfaces between different components would be constructed [20–22]. This could not only provide additional driving force for a more efficient transduction of charges through the building of an internal field [23,24], but also modulate the electronic structure and optimize adsorption energies of reaction intermediates (e.g., COOH*, CO*), which would in turn improve both the activity and selectivity of the CO_2RR catalysts [25–27]. Despite great achievements attained by this approach, the competing hydrogen evolution reaction (HER) on the surface of Ni-N-C will lead to poor CO Faradaic efficiency (FEco) during electrocatalysis in aqueous electrolytes, reducing the CO_2 conversion efficiency of Ni-N-C catalysts [28, 29]. To address this issue, it is thus enticing to explore a new class of Ni-based catalysts that can simultaneously regulate the adsorption of COOH* intermediate and inhibit HER [30].

Herein, we developed a $Ni/Ni_3ZnC_{0.7}$ heterostructured catalyst supported by porous N-doped carbon nanofibers through a cost-effective

---

electrospinning method. As shown in Fig. 1a, Ni(Ac)$_2$, Zn(Ac)$_2$ and ZnO precursors were first dispersed in the one-dimensional PAN nanofibers, followed by annealing at 900 °C under Ar atmospheres. During the pyrolysis process, porous N-doped carbon nanofibers (PNCFs) were generated after the evaporation of the Zn-containing species. At the same time, Ni/Ni$_3$ZnC$_{0.7}$ heterostructured nanoparticles were formed and uniformly embedded inside the carbon nanofibers. The as-derived Ni/Ni$_3$ZnC$_{0.7}$ electrocatalyst could achieve a high CO FE of 91.5% at −0.8 V versus reversible hydrogen electrode (vs. RHE), corresponding to 11 mA cm^{-2} partial current density of CO, which was superior to the heterostructure-free counterpart of Ni-N-C. Moreover, Ni/Ni$_3$ZnC$_{0.7}$ also demonstrated remarkable long-term stability, with 93.4% of its initial selectivity remained toward CO production after 45 h of continuous electrolysis at −0.8 V (vs. RHE). Moreover, density functional theory (DFT) calculation demonstrated that the charge transfer process was significantly enhanced at the interface, giving rise to the superior performance of Ni/Ni$_3$ZnC$_{0.7}$.

2. Experimental

2.1. Synthesis of Ni/Ni$_3$ZnC$_{0.7}$ heterostructured catalyst

Typically, PAN (1.0 g), ZnO (0.5 g), Zn(Ac)$_2$·2H$_2$O (0.5 g) and Ni (Ac)$_2$·4H$_2$O (0.4 g) powder were dissolved in 12.5 mL of DMF and stirred overnight to obtain a 8 wt% PAN solution. Next, the mixed solution was transferred into a plastic syringe (20 mL) with a 20-gauge stainless steel needle connected to a 14 kV high-voltage DC power for electrospinning. The solution flow rate and the distance between needle and tin foil collector were 1.2 mL h^{-1} and 15 cm, respectively. After that, the obtained composites film was pre-oxidized in air at 220 °C for 2 h and subsequently pyrolyzed in Ar at 900 °C for 1 h. After acid washing (1 M HCl) to remove redundant Ni and Zn species, the Ni/Ni$_3$ZnC$_{0.7}$-X was obtained. X presents the weight of Ni(Ac)$_2$·4H$_2$O in the electrospinning precursor (X = 0.4 g, 0.8 g and 1.2 g).

For comparison, all the other samples were prepared with similar method. Ni-N-C was prepared without the addition of ZnO and Zn (Ac)$_2$·2H$_2$O in the precursor. PNCF was synthesized without Ni (Ac)$_2$·4H$_2$O.
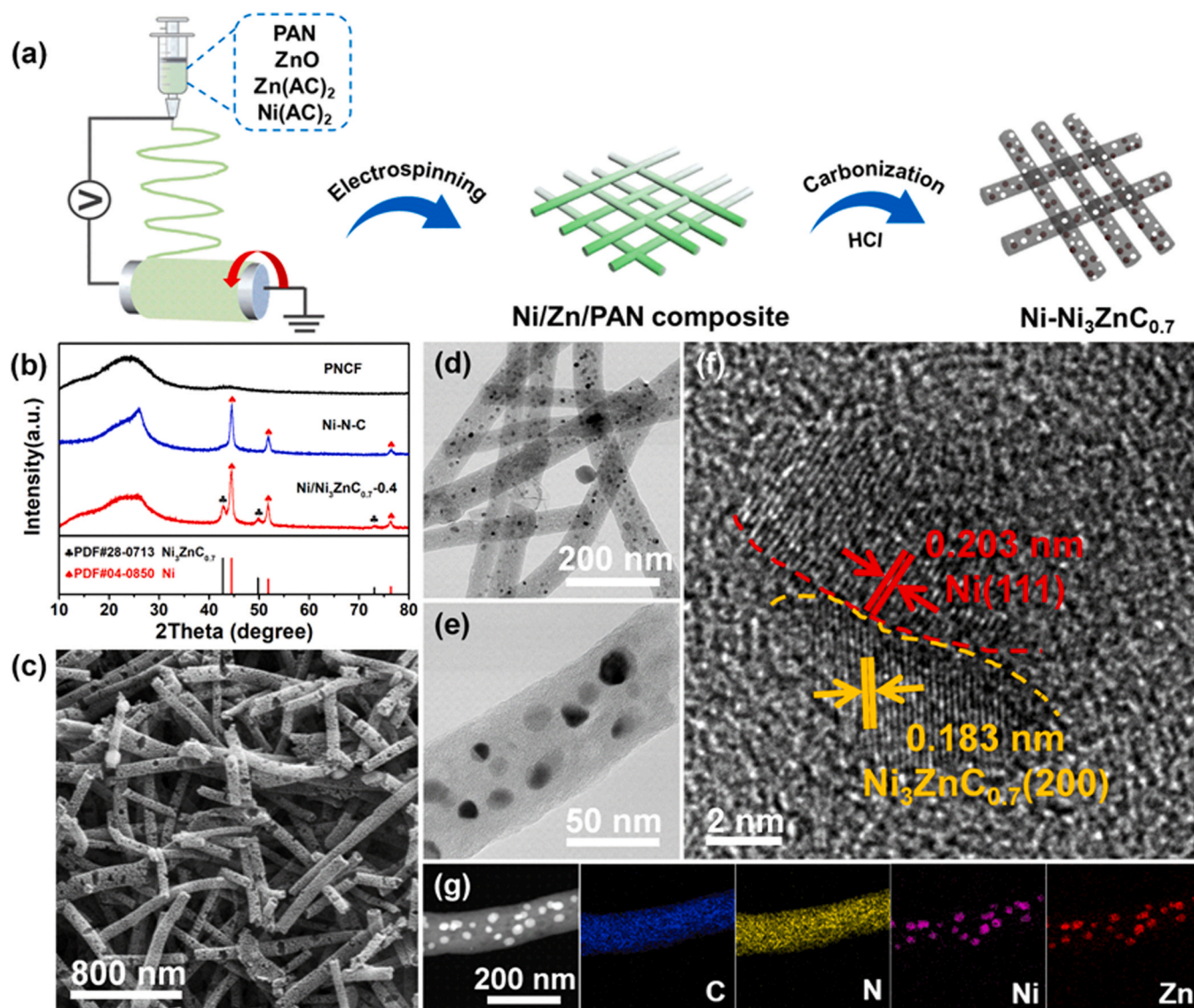

Fig. 1. (a) The schematic illustration for the preparation of Ni/Ni$_3$ZnC$_{0.7}$. (b) XRD patterns, (c) SEM image, (d, e) TEM and (f) HR-TEM image of Ni/Ni$_3$ZnC$_{0.7}$-0.4. (g) EDS mapping images of Ni/Ni$_3$ZnC$_{0.7}$-0.4.

2.2. Characterization

X-ray diffraction (XRD) patterns were characterized by Bruker D8 Advanced. Morphologies and structures of these catalysts were investigated by SEM (Phenom), TEM and HRTEM (TEM, JEM2010F). Raman spectra (Thermo Fisher DXR spectrometer) were carried out with the length of 532 nm. The pore structures of all the catalysts were measured with a surface analyzer (Kubo-X1000). X-ray photoelectron spectroscopy (XPS) was conducted on a Escalab 250Xi equipment (Thermo Fisher Scientific).

2.3. Electrochemical measurements

The linear sweep voltammetry (LSV), chronoamperometry (i-t) and long-term electrolysis tests were carried out on electrochemical workstation (CHI 760E). The CO_2RR performances of the catalyst were conducted in a two-compartment three-electrode electrochemical H-type cell. A platinum (Pt) plate and a leak-free Ag/AgCl electrode were used as the counter electrode and reference electrode, respectively.

The mixture of $Ni/Ni_3ZnC_{0.7}$ catalyst (4.5 mg), Nafion-117 solution (5 wt%, 20 μL) and ethanol (430 μL) was ultrasonically dispersed 30 min to obtain the catalyst ink. The working electrode was made by drop casting a volume of 120 μL of the homogeneous suspended liquid on one side of carbon paper (1×1.2 cm). The catalyst loading of working electrodes is 1.0 mg cm^{-2}. Each compartment contains 30 mL of 0.5 M $KHCO_3$ electrolyte solution (pH = 7.2). All the measured potentials in this word were converted into the RHE as follows:

$$E_{RHE} = E_{Ag/AgCl} + 0.244 + 0.0591 \times pH$$

During the electrochemical tests, Ar or CO_2 with a purity of 99.999% was continuously supplied to one side of the working electrode. The gas flow rate of CO_2 was controlled by a flowmeter at 20 mL min^{-1}. After continuous electrolysis at each potential for 10 min, the gas products were collected by gas chromatograph (GC, Shimadzu), and were detected and analyzed on-line by flame ionization detector (FID) and thermal conductivity detector (TCD). In addition, N_2 was used as the carrier gas. The Faradaic efficiency of CO and H_2 was calculated as the follows:

$$FE_i = \frac{Q_i}{Q} = \frac{n \times F \times P_0 \times v \times x_i}{J_{total} \times R \times T}$$

where n = 2 is the number of electrons transferred from CO_2 or water to the product (CO or H_2); F (Faradaic constant) is 96,485 C mol^{-1}; P_0 (ambient pressure) is 1.013×10^5 Pa; v (CO_2 flow rate) is 20 sccm; x_i is the volume fraction of CO or H_2; J_{total} is the total current density; R (ideal gas constant) is 8.314 J mol^{-1} K^{-1} and T (room temperature) is 25 ℃.

2.4. Computational details

Density functional theory (DFT) calculations were performed by combining the DFT method with the Vienna Ab-Initio Simulation Package (VASP) [31,32]. Projected augmented wave (PAW) was employed for revealing the ion-electron interactions. The electron-electron interactions was described by Perdew-Burke-Ernzerhof (PBE) functional [33]. An energy cutoff of 450 eV was used. The Brillourin zone was sampled with a gamma-centered grid $3 \times 3 \times 1$ for geometry optimization and $6 \times 6 \times 1$ for self-consistent iteration of single point energy and charge density difference calculation. The force and energy were converged to 0.02 eV Å^{-1} and 2.0×10^{-5} eV, respectively. In order to correct the strong interactions between electrons in 3d orbitals of transition metals, all calculations were spin polarized and DFT+U method was adopted. The U-J values of Ni and Zn were set to 5.4 and 3.7 eV, respectively. The (001) and (010) plane of Ni and $Ni_3ZnC_{0.7}$ were adopted, respectively, to construct heterostructure. The models of $Ni/Ni_3ZnC_{0.7}$-0.4 and pure Ni

were established by a 2×2 supercell. A vacuum space of 20 Å was set to avoid interaction between adjacent layers. Herein, the CO_2RR reaction mechanism was considered as followed:

$$CO_2 + (H^+ + e^-) + * \rightarrow COOH^*$$

$$COOH^* + (H^+ + e^-) + * \rightarrow CO^* + H_2O$$

$$CO^* \rightarrow CO + *$$
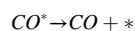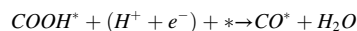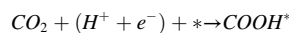
where the asterisk (*) represents the active site of surface substrate. The Gibbs free energies of CO_2RR were calculated at 298.15 K, according to the following equation:

$$\Delta G_{ads} = \Delta E_{ads} - T\Delta S_{ads} + \Delta E_{ZPE}$$

where ΔE_{ads}, ΔS_{ads}, and ΔE_{ZPE} are the energy change, reaction entropy change correction, and zero-point energy, respectively.

3. Results and discussion

3.1. Catalyst characterization

Fig. 1b exhibited the X-ray diffraction (XRD) patterns of PNCF, Ni-N-C and $Ni/Ni_3ZnC_{0.7}$-0.4. The PNCF displayed two broad peaks at 24° and 44° corresponding to the (002) and (101) planes of graphitic carbon, respectively. Three sharp peaks at around 44.5°, 49.8° and 73.1° can be assigned to the (111), (200) and (220) planes of metallic Ni, respectively, indicating that Ni nanoparticles were appeared in both $Ni/Ni_3ZnC_{0.7}$-X (X = 0.2, 0.4 and 0.8) and Ni-N-C samples. With the zinc species in the precursor, three diffraction peaks located at approximately 42.8°, 51.8° and 76.4°, attributing to the (111), (200) and (220) crystal planes of $Ni_3ZnC_{0.7}$, respectively, were observed, thus suggesting the successful preparation of a composite consisting of both Ni and $Ni_3ZnC_{0.7}$ (Fig. S1).

The morphologies of PNCF, Ni-N-C and $Ni/Ni_3ZnC_{0.7}$ were first investigated by scanning electron microscopy (SEM), and all samples showed uniform fiber-like structure (Figs. 1c and S2) with several micrometers in length and 60–150 nm in diameter. Moreover, the rough surface of $Ni/Ni_3ZnC_{0.7}$-0.4 could be attributed to the presence of pores which were formed by the evaporation of the Zn species during pyrolysis. The corresponding transmission electron microscopy (TEM) image revealed that nanoparticles with an average size of ∼ 12.2 nm were evenly embedded in the porous carbon fibers (Figs. 1d, 1e and S3). Subsequently, the lattice fringes with interplanar distances of ∼ 0.203 and ∼ 0.183 nm in the high-resolution TEM (HR-TEM; Fig. 1f) can be ascribed to the (200) plane of $Ni_3ZnC_{0.7}$ and (111) plane of Ni, respectively. This gave rise to distinct interface of the heterostructure consisting of these two phases. Furthermore, the energy-dispersive X-ray spectroscopy (EDS) mapping revealed that the N and C elements were uniformly distributed in the carbon nanofibers (Fig. 1g), while Ni and Zn overlap with each other, coincide with the presence of the nanoparticles.

Raman spectroscopy was performed to obtain the structural information of these samples. As depicted in Fig. 2a, all samples had two peaks at around 1340 cm^{-1} and 1590 cm^{-1} corresponding to the D and G band, respectively. The intensity ratios (I_D/I_G) of PNCF and $Ni/Ni_3ZnC_{0.7}$-0.4 were calculated to be 0.98 and 0.96, indicating that abundant defects were generated in the composite sample due to the addition of the Zn species. A higher graphitization degree was detected for Ni-N-C (I_D/I_G=0.95), probably attributing to the catalytic effect of the Ni nanoparticles [34,35]. The surface structure of these samples was characterized by the nitrogen adsorption-desorption measurement. It is clear from Fig. 2b and Fig. S4 that $Ni/Ni_3ZnC_{0.7}$-X, PNCF and Ni-N-C exhibited a typical type IV isotherm curve with H1 hysteresis loop, which was an indicator of the mesoporous structure. Owing to the evaporation of the Zn species, the specific surface areas of $Ni/Ni_3ZnC_{0.7}$ (469.3 m^2 g^{-1} for $Ni/Ni_3ZnC_{0.7}$-0.2, 558.8 m^2 g^{-1} for $Ni/Ni_3ZnC_{0.7}$-0.4
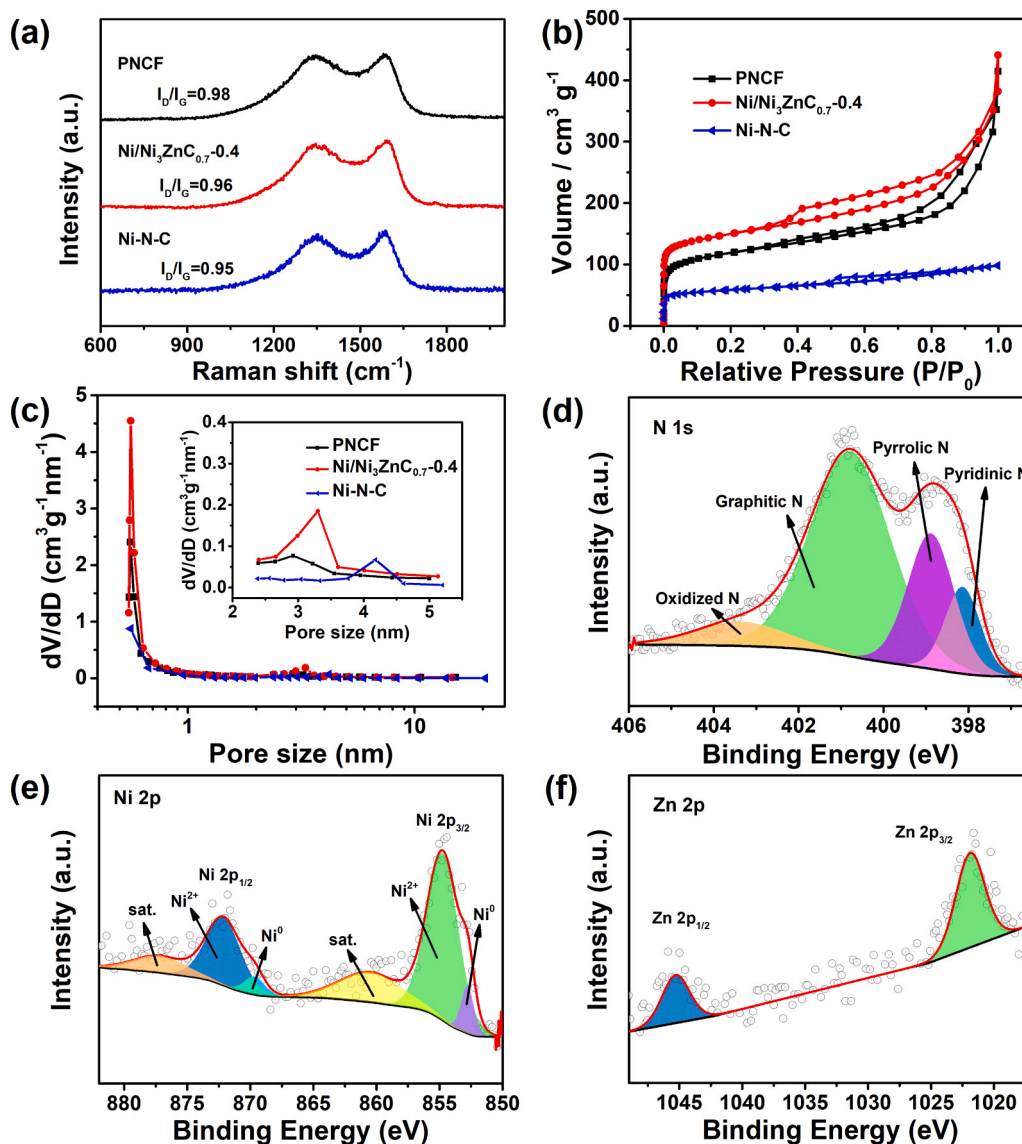
Fig. 2. (a) Raman spectra, (b) N_2 adsorption-desorption isotherms and (c) pore size distribution of PNCF, Ni-$Ni_3ZnC_{0.7}$-0.4 and Ni-N-C. The inset is an enlarged view with a pore size of approximately 2–5.5 nm. High-resolution XPS spectra of Ni-$Ni_3ZnC_{0.7}$-0.4: (d) N 1s, (e) Ni 2p and (f) Zn 2p.

and 469.2 m^2 g^{-1} for Ni/$Ni_3ZnC_{0.7}$-0.8) and PNCF (433.8 m^2 g^{-1}) were much higher than that of Ni-N-C (219.2 m^2 g^{-1}). In addition, the pore size distributions displayed that all samples possessed two peaks concentrated at 0.5 nm and 3.5 nm, and Ni/$Ni_3ZnC_{0.7}$-0.4 had the largest pore volumes (Fig. 2c and Table S2). The high specific surface area and abundant mesopores of Ni/$Ni_3ZnC_{0.7}$-0.4 would be beneficial for facilitating mass transport and exposing more active sites for CO_2RR [4,36].

The elemental composition and chemical state of these as-obtained samples were further analyzed by X-ray photoelectron spectroscopy (XPS). It was evident that all samples contained C, N, and O (Fig. S5). The PNCF and Ni-N-C catalysts possessed Zn and Ni, respectively, while Ni/$Ni_3ZnC_{0.7}$-0.4 possessed both these metal elements and the content of each element were shown in Table S3 [37,38]. As shown in Figs. 2d and S6, the high-resolution N 1s spectra of Ni/$Ni_3ZnC_{0.7}$-0.4, PNCF and Ni-N-C can be fitted to pyridinic N ($\sim$ 398.2 eV), pyrrolic N ($\sim$ 400.5 eV), graphitic N ($\sim$ 401.3 eV) and oxidized N ($\sim$ 403.0 eV) [9, 39]. The high-resolution Ni 2p spectrum of Ni/$Ni_3ZnC_{0.7}$-0.4 displayed two peaks at 852.7 eV (Ni 2p3/2) and 869.6 eV (Ni 2p1/2) corresponding to Ni^0, revealing the presence of metallic Ni, which was consistent with the XRD results (Figs. 1b and 2e) [40]. Furthermore, the

peaks at 854.8 eV (Ni 2p3/2) and 872.2 eV (Ni 2p1/2) representing characteristic peaks of oxidized Ni species were obviously detected [39, 41]. Compared with Ni-N-C, the Ni 2p1/2 and Ni 2p3/2 peaks in Ni/$Ni_3ZnC_{0.7}$-0.4 were negatively shifted, which may be beneficial to the activation of CO_2 molecules (Fig. S7) [42]. In addition, the Zn 2p spectra of Ni/$Ni_3ZnC_{0.7}$-0.4 and PNCF exhibited two characteristic peaks attributing to Zn 2p3/2 at 1022 eV and Zn 2p1/2 at 1045 eV (Figs. 2f, S8) [43,44].

3.2. Electrochemical performance

The electrocatalytic performances of PNCF, Ni-N-C and Ni/$Ni_3ZnC_{0.7}$-0.4 were first evaluated by LSV in an H-type electrochemical cell with CO_2-saturated 0.5 M $KHCO_3$ electrolyte. As shown in Figs. 3a and S9a, all samples presented higher current density (j) in CO_2-saturated electrolyte from −0.5 V to −1.1 V vs. RHE, which were significantly exceeded that in Ar-saturated electrolyte, indicating that all the catalysts are electrochemically active toward CO_2RR. Particularly, Ni/$Ni_3ZnC_{0.7}$-0.4 exhibited the highest current density at all applied potentials among all samples, and it reached a current density of 25.1 mA cm^{-2} at −1.0 V, which was superior to that of PNCF
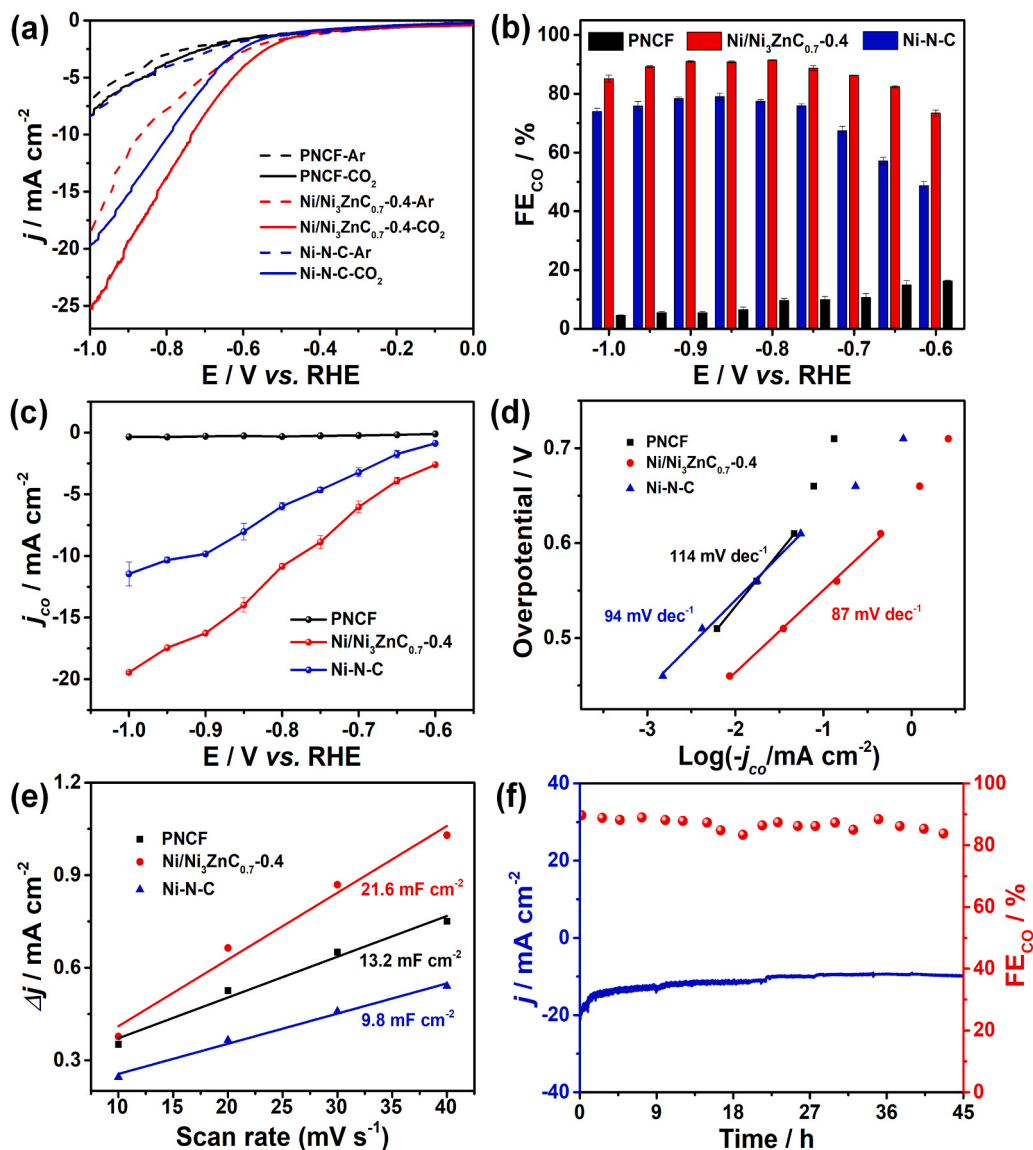
Fig. 3. (a) LSV curves for PNCF, Ni/Ni$_3$ZnC$_{0.7}$-0.4 and Ni-N-C in 0.5 M CO$_2$-saturated KHCO$_3$ electrolyte. (b) FE$_{CO}$ at different potentials, (c) j_{co} for all samples at various potentials, (d) Tafel plots and (e) Electrochemical double layer capacitance measurements for PNCF, Ni/Ni$_3$ZnC$_{0.7}$-0.4 and Ni-N-C. (f) Long-term stability of Ni/Ni$_3$ZnC$_{0.7}$-0.4 at −0.8 V vs. RHE.

(8.3 mA cm^{-2}) and Ni-N-C (19.7 mA cm^{-2}).

Next, gas chromatography (GC) was used to detect the gas products of the catalyst after 30 min of stable operation from −0.6 V to −1.0 V (Fig. S10). H$_2$ and CO were the dominant products observed by GC. The electrolyte was subjected to ^{1}H nuclear magnetic resonance (NMR) detection, and no liquid product was detected (Fig. S11). The corresponding FE$_{CO}$ of Ni/Ni$_3$ZnC$_{0.7}$-0.4 was displayed in Fig. 3b, and it exceeds 86% in the potential range of −0.7 V to −0.95 V vs. RHE, with a maximal value of 91.5% at −0.8 V vs. RHE, while Ni-N-C and PNCF exhibit poorer CO$_2$RR performance in the same potential range, with the highest FE$_{CO}$ of only 80.0% and 16.4%, respectively. The total FE$_{CO}$ of these three samples was also shown in Fig. S12. The partial current density of CO (j_{CO}) at all applied potentials was calculated in Fig. 3c. At −0.8 V, j_{CO} of Ni/Ni$_3$ZnC$_{0.7}$-0.4 is −11 mA cm^{-2}, which is about 1.8 times and 33.9 times higher than those of Ni-N-C and PNCF, respectively, and is also higher than those of Ni/Ni$_3$ZnC$_{0.7}$-0.2 and Ni/Ni$_3$ZnC$_{0.7}$-0.8 (Fig. S9b and c).

To assess the reaction kinetics, the Tafel plots were analyzed, showing values of 87 mV dec^{-1} and 94 mV dec^{-1} for Ni/Ni$_3$ZnC$_{0.7}$-0.4 and Ni-N-C, respectively, which were much lower than PNCF (114 mV

dec^{-1}) and other Ni/Ni$_3$ZnC$_{0.7}$ counterparts (Figs. 3d and S9d), implying that the first electron transfer to generate COOH* intermediate is the rate-determining step (RDS) in both Ni/Ni$_3$ZnC$_{0.7}$-0.4 and Ni-N-C [6,40, 45]. Fig. S13 showed the slope of the double-layer current and the corresponding scan rate, which can reflect the electrochemically active surface area (ECSA). The calculated specific capacitance (Cs) of smooth carbon paper is 0.9 mF cm^{-2} (Fig. S14), and the double layer capacitance (C$_{dl}$) was 21.6 mF cm^{-2} for Ni/Ni$_3$ZnC$_{0.7}$-0.4, which was roughly 2.2 and 1.64 times higher than those of Ni-N-C (9.8 mF cm^{-2}) and PNCF (13.2 mF cm^{-2}) (Fig. 3e and Table S2). It indicated that the construction of Ni/Ni$_3$ZnC$_{0.7}$ heterostructure could offer more accessible active sites during the CO$_2$ electroreduction process, playing a key role in enhancing its catalytic activity. Moreover, both the specific surface area and ECSA of Ni/Ni$_3$ZnC$_{0.7}$-0.4 were much higher than those of Ni/Ni$_3$ZnC$_{0.7}$-0.2 and Ni/Ni$_3$ZnC$_{0.7}$-0.8, giving rise to a higher current density and FEco. Furthermore, electrochemical impedance spectroscopy (EIS) results showed that the charge transfer resistance (R$_{CT}$) of Ni/Ni$_3$ZnC$_{0.7}$-0.4 was 18.8 Ω, which was lower than PNCF and Ni-N-C (Fig. S15, Table S1), indicating that the Ni/Ni$_3$ZnC$_{0.7}$ heterostructure greatly promotes electron transfer and contributes to accelerating kinetics. Stability is

another key factor determining the feasibility of the catalyst for practical applications, which has been subsequently examined at − 0.8 V vs. RHE. Encouragingly, $Ni/Ni_3ZnC_{0.7}$-0.4 maintains 93.4% of its initial FE_{CO} with a current density of about 10 mA cm^{-2} after 45 h of continuous electrolysis (Fig. 3f), showing excellent long-term stability. In addition, the morphologies of the nanofibers have retained without any structural collapse after electrolysis (Fig. S16), demonstrating great potential for practical application.

3.3. Theoretical computation

In order to elucidate the origin of the outstanding CO_2RR performance of $Ni/Ni_3ZnC_{0.7}$-0.4, the first principal calculations were conducted. Based on the XRD results, two models of $Ni/Ni_3ZnC_{0.7}$ heterostructure and pure Ni were established (Fig. S17). The Gibbs free energy diagrams of $Ni/Ni_3ZnC_{0.7}$ and Ni in Fig. 4a revealed that the formation of COOH* could be considered as the RDS of the two models, which was consistent with the results of Tafel analysis. Apparently, $Ni/Ni_3ZnC_{0.7}$ exhibited an endothermic energy barrier of 1.35 eV, which was significantly lower than that of pure Ni model (1.93 eV), indicating that this RDS was facilitated by the heterostructure [40]. In addition, the $Ni/Ni_3ZnC_{0.7}$ displayed a higher free energy change for H* formation of 0.27 eV compared to pure Ni (0.13 eV), suggesting that the competing HER process could be suppressed in $Ni/Ni_3ZnC_{0.7}$ (Fig. 4b) [39]. The charge density difference for COOH* adsorption on $Ni/Ni_3ZnC_{0.7}$ and pure Ni was further investigated. Fig. 4c presented that the heterostructure showed intensive electron density depletion and accumulation, suggesting an enhanced charge transfer than that of pure Ni [46]. Moreover, the calculated density of states (DOS) illustrated that the *d*-band center of $Ni/Ni_3ZnC_{0.7}$ displayed a upshift of 0.14 eV after adsorbing COOH*, while an downshift was taking place in pure Ni, suggesting more electrons transferred between $Ni/Ni_3ZnC_{0.7}$ and

COOH* [47]. On the contrary, the *d*-band center of Ni showed an upshift of 0.02 eV after adsorbing H*, while that of $Ni/Ni_3ZnC_{0.7}$ remained unchanged, which further suggested that HER process could be suppressed on the $Ni/Ni_3ZnC_{0.7}$.

4. Conclusion

In summary, we reported an electrospinning strategy to construct $Ni/Ni_3ZnC_{0.7}$ heterostructured nanoparticles embedded in porous carbon nanofibers as an efficient electrocatalyst towards CO_2RR. The $Ni/Ni_3ZnC_{0.7}$-0.4 catalyst exhibited a remarkable FE_{CO} of 91.5% at −0.8 V vs. RHE, an excellent partial current of 11 mA cm^{-2} at this potential, and a superior long-term stability for 45 h of continuous electrolysis. DFT calculations have confirmed that the existence of $Ni/Ni_3ZnC_{0.7}$ heterostructure played a key role in reducing the energy barrier for the formation of COOH* intermediates, promoting a more efficient CO_2RR process. By introducing the heterostructure of Ni and $Ni_3ZnC_{0.7}$, this work developed a facile approach to prepare high-performance Ni-based electrocatalysts for CO_2RR, which could also be extended to fabricate other types of active materials for a wide range of electrochemical applications.

CRediT authorship contribution statement

Xinxin Wei: Conceptualization, Investigation, Writing – review & editing, Visualization. **Shuhao Xiao:** Conceptualization, Methodology, Writing – review & editing, Visualization. **Rui Wu:** Conceptualization, Supervision, Writing – guidance & revision, Project administration, Funding acquisition. **Zhaozhao Zhu:** Discussion, Revision. **Lei Zhao:** Data curation, Formal analysis. **Zhao Li:** Data curation. **Junjie Wang:** Data curation. **Jun Song Chen:** Supervision, Revision, Project administration, Funding acquisition. **Zidong Wei:** Supervision, Revision,
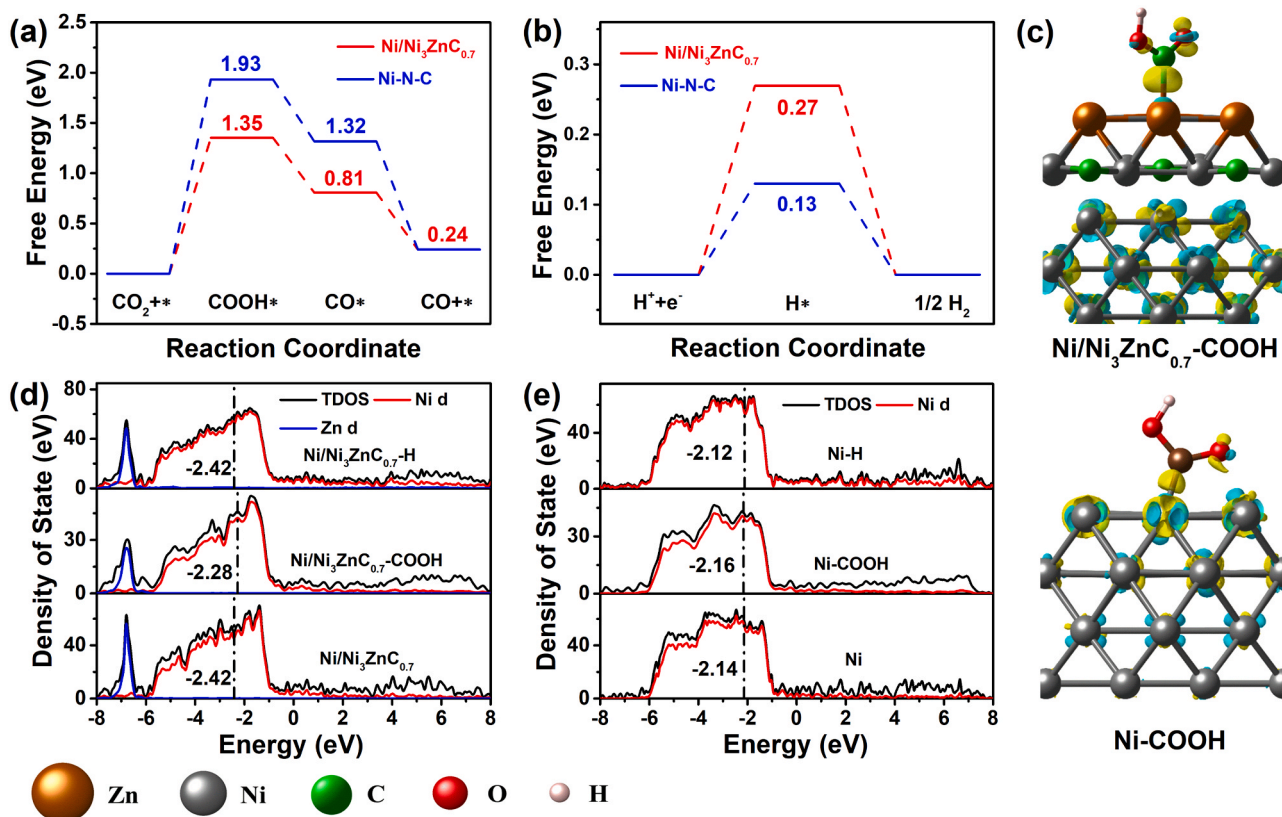

Fig. 4. Gibbs free energy diagrams for (a) CO_2 reduction to CO and (b) HER on $Ni/Ni_3ZnC_{0.7}$-0.4 and Ni-N-C. (c) The difference of electron density for COOH* intermediates adsorbed on $Ni/Ni_3ZnC_{0.7}$ and pure Ni. Calculated DOS and d-states of the optimized structures for (d) $Ni/Ni_3ZnC_{0.7}$ and (e) Ni-N-C.

Appendix A. Supplementary material

Supplementary data associated with this article can be found in the online version at doi:10.1016/j.apcatb.2021.120861.

References

[1] H.B. Yang, S.-F. Hung, S. Liu, K. Yuan, S. Miao, L. Zhang, X. Huang, H.-Y. Wang, W. Cai, R. Chen, J. Gao, X. Yang, W. Chen, Y. Huang, H.M. Chen, C.M. Li, T. Zhang, B. Liu, Atomically dispersed Ni(i) as the active site for electrochemical CO₂ reduction, Nat. Energy 3 (2018) 140–147, https://doi.org/10.1038/s41560-017-0078-8.
[2] J.T. Billy, A.C. Co, Reducing the onset potential of CO₂ electroreduction on CuRu bimetallic particles, Appl. Catal. B 237 (2018) 911–918, https://doi.org/10.1016/j.apcatb.2018.06.072.
[3] T. Zheng, K. Jiang, N. Ta, Y. Hu, J. Zeng, J. Liu, H. Wang, Large-scale and highly selective CO₂ electrocatalytic reduction on nickel single-atom catalyst, Joule 3 (2019) 265–278, https://doi.org/10.1016/j.joule.2018.10.015.
[4] B. Wei, Y. Xiong, Z. Zhang, J. Hao, L. Li, W. Shi, Efficient electrocatalytic reduction of CO₂ to HCOOH by bimetallic In-Cu nanoparticles with controlled growth facet, Appl. Catal. B 283 (2021), 119646, https://doi.org/10.1016/j.apcatb.2020.119646.
[5] K. Jiang, S. Siahrostami, T. Zheng, Y. Hu, S. Hwang, E. Stavitski, Y. Peng, J. Dynes, M. Gangisetty, D. Su, K. Attenkofer, H. Wang, Isolated Ni single atoms in graphene nanosheets for high-performance CO₂ reduction, Energy Environ. Sci. 11 (2018) 893–903, https://doi.org/10.1039/C7EE03245E.
[6] W. Ren, X. Tan, W. Yang, C. Jia, S. Xu, K. Wang, S.C. Smith, C. Zhao, Isolated diatomic Ni-Fe metal-nitrogen sites for synergistic electroreduction of CO₂, Angew. Chem. Int. Ed. 58 (2019) 6972–6976, https://doi.org/10.1002/anie.201901575.
[7] Z. Chen, M.-R. Gao, N. Duan, J. Zhang, Y.-Q. Zhang, T. Fan, J. Zhang, Y. Dong, J. Li, Q. Liu, X. Yi, J.-L. Luo, Tuning adsorption strength of CO₂ and its intermediates on tin oxide-based electrocatalyst for efficient CO₂ reduction towards carbonaceous products, Appl. Catal. B 277 (2020), 119252, https://doi.org/10.1016/j.apcatb.2020.119252.
[8] C. Lu, J. Yang, S. Wei, S. Bi, Y. Xia, M. Chen, Y. Hou, M. Qiu, C. Yuan, Y. Su, F. Zhang, H. Liang, X. Zhuang, Atomic Ni anchored covalent triazine framework as high efficient electrocatalyst for carbon dioxide conversion, Adv. Funct. Mater. 29 (2019), 1806884, https://doi.org/10.1002/adfm.201806884.
[9] Q. Fan, P. Hou, C. Choi, T.-S. Wu, S. Hong, F. Li, Y.-L. Soo, P. Kang, Y. Jung, Z. Sun, Activation of Ni particles into single Ni-N atoms for efficient electrochemical reduction of CO₂, Adv. Energy Mater. 10 (2020), 1903068, https://doi.org/10.1002/aenm.201903068.
[10] F. Pan, H. Zhang, Z. Liu, D. Cullen, K. Liu, K. More, G. Wu, G. Wang, Y. Li, Atomic-level active sites of efficient imidazolate framework-derived nickel catalysts for CO₂ reduction, J. Mater. Chem. A 7 (2019) 26231–26237, https://doi.org/10.1039/C9TA08862H.
[11] Y. Hou, Y.-L. Liang, P.-C. Shi, Y.-B. Huang, R. Cao, Atomically dispersed Ni species on N-doped carbon nanotubes for electroreduction of CO₂ with nearly 100% CO selectivity, Appl. Catal. B 271 (2020), 118929, https://doi.org/10.1016/j.apcatb.2020.118929.
[12] Y. Chen, Y. Yao, Y. Xia, K. Mao, G. Tang, Q. Wu, L. Yang, X. Wang, X. Sun, Z. Hu, Advanced Ni-Nₓ-C single-site catalysts for CO₂ electroreduction to CO based on hierarchical carbon nanocages and S-doping, Nano Res. 13 (2020) 2777–2783, https://doi.org/10.1007/s12274-020-2928-0.
[13] H. Yang, L. Shang, Q. Zhang, R. Shi, G.I.N. Waterhouse, L. Gu, T. Zhang, A universal ligand mediated method for large scale synthesis of transition metal single atom catalysts, Nat. Commun. 10 (2019) 4585, https://doi.org/10.1038/s41467-019-12510-0.
[14] Y.-N. Gong, L. Jiao, Y. Qian, C.-Y. Pan, L. Zheng, X. Cai, B. Liu, S.-H. Yu, H.-L. Jiang, Regulating the coordination environment of MOF-templated single-atom nickel electrocatalysts for boosting CO₂ reduction, Angew. Chem. Int. Ed. 59 (2020) 2705–2709, https://doi.org/10.1002/anie.201914977.
[15] Y. Cheng, S. Zhao, B. Johannessen, J.-P. Veder, M. Saunders, M.R. Rowles, M. Cheng, C. Liu, M.F. Chisholm, R. De Marco, H.-M. Cheng, S.-Z. Yang, S.P. Jiang, Atomically dispersed transition metals on carbon nanotubes with ultrahigh loading

[16] P. Lu, J. Zhang, H. He, M. Wang, Z. Luo, D. Gao, Z. Liu, X. Wang, M. Yuan, S. Dipazir, H. Zhao, Y. Xie, G. Zhang, Iron/nickel nano-alloy encapsulated in nitrogen-doped carbon framework for CO₂ electrochemical conversion with prominent CO selectivity, J. Power Sources 449 (2020), 227496, https://doi.org/10.1016/j.jpowsour.2019.227496.
[17] Y. Cheng, S. Zhao, H. Li, S. He, J.-P. Veder, B. Johannessen, J. Xiao, S. Lu, J. Pan, M.F. Chisholm, S.-Z. Yang, C. Liu, J.G. Chen, S.P. Jiang, Unsaturated edge-anchored Ni single atoms on porous microwave exfoliated graphene oxide for electrochemical CO₂, Appl. Catal. B 243 (2019) 294–303, https://doi.org/10.1016/j.apcatb.2018.10.046.
[18] W. Kou, Y. Zhang, J. Dong, C. Mu, L. Xu, Nickel-nitrogen-doped three-dimensional ordered macro-/mesoporous carbon as an efficient electrocatalyst for CO₂ reduction to CO, ACS Appl. Energy Mater. 3 (2020) 1875–1882, https://doi.org/10.1021/acsaem.9b02324.
[19] P. Lu, Y. Yang, J. Yao, M. Wang, S. Dipazir, M. Yuan, J. Zhang, X. Wang, Z. Xie, G. Zhang, Facile synthesis of single-nickel-atomic dispersed N-doped carbon framework for efficient electrochemical CO₂ reduction, Appl. Catal. B 241 (2019) 113–119, https://doi.org/10.1016/j.apcatb.2018.09.025.
[20] H. Yang, Y.-w. Hu, J.-j. Chen, M.S. Balogun, P.-p. Fang, S. Zhang, J. Chen, Y. Tong, Intermediates adsorption engineering of CO₂ electroreduction reaction in highly selective heterostructure Cu-based electrocatalysts for CO production, Adv. Energy Mater. 9 (2019), 1901396, https://doi.org/10.1002/aenm.201901396.
[21] P. Wang, M. Qiao, Q. Shao, Y. Pi, X. Zhu, Y. Li, X. Huang, Phase and structure engineering of copper tin heterostructures for efficient electrochemical carbon dioxide reduction, Nat. Commun. 9 (2018) 4933, https://doi.org/10.1038/s41467-018-07419-z.
[22] J.-F. Xie, J.-J. Chen, Y.-X. Huang, X. Zhang, W.-K. Wang, G.-X. Huang, H.-Q. Yu, Selective electrochemical CO₂ reduction on Cu-Pd heterostructure, Appl. Catal. B 270 (2020), 118864, https://doi.org/10.1016/j.apcatb.2020.118864.
[23] L. Guo, Z. Yang, K. Marcus, Z. Li, B. Luo, L. Zhou, X. Wang, Y. Du, Y. Yang, MoS₂/TiO₂ heterostructures as nonmetal plasmonic photocatalysts for highly efficient hydrogen evolution, Energy Environ. Sci. 11 (2018) 106–114, https://doi.org/10.1039/C7EE02464A.
[24] K. Wang, D. Liu, P. Deng, L. Liu, S. Lu, Z. Sun, Y. Ma, Y. Wang, M. Li, B.Y. Xia, C. Xiao, S. Ding, Band alignment in Zn₂SnO₄/SnO₂ heterostructure enabling efficient CO₂ electrochemical reduction, Nano Energy 64 (2019) 103954, https://doi.org/10.1016/j.nanoen.2019.103954.
[25] Q. Qian, J. Zhang, J. Li, Y. Li, X. Jin, Y. Zhu, Y. Liu, Z. Li, A. El-Harairy, C. Xiao, G. Zhang, Y. Xie, Artificial heterointerfaces achieve delicate reaction kinetics towards hydrogen evolution and hydrazine oxidation catalysis, Angew. Chem. Int. Ed. 60 (2021) 5984–5993, https://doi.org/10.1002/anie.202014362.
[26] X. Li, Y. Wang, J. Wang, Y. Da, J. Zhang, L. Li, C. Zhong, Y. Deng, X. Han, W. Hu, Sequential electrodeposition of bifunctional catalytically active structures in MoO₃/Ni-NiO composite electrocatalysts for selective hydrogen and oxygen evolution, Adv. Mater. 32 (2020), 2003414, https://doi.org/10.1002/adma.202003414.
[27] Y.-W. Peng, C. Shan, H.-J. Wang, L.-Y. Hong, S. Yao, R.-J. Wu, Z.-M. Zhang, T.-B. Lu, Polyoxometalate-derived ultrasmall Pt₂W/WO₃ heterostructure outperforms platinum for large-current-density H₂ evolution, Adv. Energy Mater. 9 (2019), 1900597, https://doi.org/10.1002/aenm.201900597.
[28] Y.J. Sa, Y. Jung, D. Shin, H.Y. Jeong, S. Ringe, H. Kim, Y.J. Hwang, S.H. Joo, Thermal transformation of molecular Ni²⁺-N₄ sites for enhanced CO₂ electroreduction activity, ACS Catal. 10 (2020) 10920–10931, https://doi.org/10.1021/acscatal.0c02325.
[29] C.F. Wen, F. Mao, Y. Liu, X.Y. Zhang, H.Q. Fu, L.R. Zheng, P.F. Liu, H.G. Yang, Nitrogen-stabilized low-valent Ni motifs for efficient CO₂ electrocatalysis, ACS Catal. 10 (2020) 1086–1093, https://doi.org/10.1021/acscatal.9b02978.
[30] C. Yan, H. Li, Y. Ye, H. Wu, F. Cai, R. Si, J. Xiao, S. Miao, S. Xie, F. Yang, Y. Li, G. Wang, X. Bao, Coordinatively unsaturated nickel-nitrogen sites towards selective and high-rate CO₂ electroreduction, Energy Environ. Sci. 11 (2018) 1204–1210, https://doi.org/10.1039/C8EE00133B.
[31] P.E. Blöchl, Projector augmented-wave method, Phys. Rev. B 50 (1994) 17953–17979, https://doi.org/10.1103/PhysRevB.50.17953.
[32] G. Kresse, J. Furthmüller, Efficient iterative schemes for ab initio total-energy calculations using a plane-wave basis set, Phys. Rev. B 54 (1996) 11169–11186, https://doi.org/10.1103/PhysRevB.54.11169.
[33] J.P. Perdew, K. Burke, M. Ernzerhof, Generalized gradient approximation made simple, Phys. Rev. Lett. 77 (1996) 3865–3868, https://doi.org/10.1103/PhysRevLett.77.3865.
[34] Z. Ma, X. Zhang, D. Wu, X. Han, L. Zhang, H. Wang, F. Xu, Z. Gao, K. Jiang, Ni and nitrogen-codoped ultrathin carbon nanosheets with strong bonding sites for efficient CO₂ electrochemical reduction, J. Colloid Interface Sci. 570 (2020) 31–40, https://doi.org/10.1016/j.jcis.2020.02.050.
[35] Z. Ma, D. Wu, X. Han, H. Wang, L. Zhang, Z. Gao, F. Xu, K. Jiang, Ultrasonic assisted synthesis of Zn-Ni bi-metal MOFs for interconnected Ni-N-C materials with enhanced electrochemical reduction of CO₂, J. CO₂ Util. 32 (2019) 251–258, https://doi.org/10.1016/j.jcou.2019.04.006.
[36] H. Yang, Q. Lin, C. Zhang, X. Yu, Z. Cheng, G. Li, Q. Hu, X. Ren, Q. Zhang, J. Liu, C. He, Carbon dioxide electroreduction on single-atom nickel decorated carbon membranes with industry compatible current densities, Nat. Commun. 11 (2020) 593, https://doi.org/10.1038/s41467-020-14402-0.
[37] A. Rendón-Calle, Q.H. Low, S.H.L. Hong, S. Builes, B.S. Yeo, F. Calle-Vallejo, How symmetry factors cause potential- and facet-dependent pathway shifts during CO₂

reduction to CH_4 on Cu electrodes, Appl. Catal. B 285 (2021), 119776, https://doi.org/10.1016/j.apcatb.2020.119776.

[38] C.-Z. Yuan, L.-Y. Zhan, S.-J. Liu, F. Chen, H. Lin, X.-L. Wu, J. Chen, Semi-sacrificial template synthesis of single-atom Ni sites supported on hollow carbon nanospheres for efficient and stable electrochemical CO_2 reduction, Inorg. Chem. Front. 7 (2020) 1719–1725, https://doi.org/10.1039/C9QI01688K.

[39] M. Jia, C. Choi, T.-S. Wu, C. Ma, P. Kang, H. Tao, Q. Fan, S. Hong, S. Liu, Y.-L. Soo, Y. Jung, J. Qiu, Z. Sun, Carbon-supported Ni nanoparticles for efficient CO_2 electroreduction, Chem. Sci. 9 (2018) 8775–8780, https://doi.org/10.1039/C8SC03732A.

[40] C.-Z. Yuan, H.-B. Li, Y.-F. Jiang, K. Liang, S.-J. Zhao, X.-X. Fang, L.-B. Ma, T. Zhao, C. Lin, A.-W. Xu, Tuning the activity of N-doped carbon for CO_2 reduction via in situ encapsulation of nickel nanoparticles into nano-hybrid carbon substrates, J. Mater. Chem. A 7 (2019) 6894–6900, https://doi.org/10.1039/C8TA11500A.

[41] R. Li, X. Li, D. Yu, L. Li, G. Yang, K. Zhang, S. Ramakrishna, L. Xie, S. Peng, $Ni_3ZnC_{0.7}$ nanodots decorating nitrogen-doped carbon nanotube arrays as a self-standing bifunctional electrocatalyst for water splitting, Carbon 148 (2019) 496–503, https://doi.org/10.1016/j.carbon.2019.04.002.

[42] S. Ma, P. Su, W. Huang, S.P. Jiang, S. Bai, J. Liu, Atomic Ni species anchored N-doped carbon hollow spheres as nanoreactors for efficient electrochemical CO_2

[43] reduction, ChemCatChem 11 (2019) 6092–6098, https://doi.org/10.1002/cctc.201901643.

[44] K. Liu, J. Wang, M. Shi, J. Yan, Q. Jiang, Simultaneous achieving of high faradaic efficiency and CO partial current density for CO_2 reduction via robust, noble-metal-free Zn nanosheets with favorable adsorption energy, Adv. Energy Mater. 9 (2019), 1900276, https://doi.org/10.1002/aenm.201900276.

[44] Y. Dou, A. Zhou, Y. Yao, S.Y. Lim, J.-R. Li, W. Zhang, Suppressing hydrogen evolution for high selective CO_2 reduction through surface-reconstructed heterojunction photocatalyst, Appl. Catal. B 286 (2021), 119876, https://doi.org/10.1016/j.apcatb.2021.119876.

[45] F. Li, L. Chen, G.P. Knowles, D.R. MacFarlane, J. Zhang, Hierarchical mesoporous SnO_2 nanosheets on carbon cloth: a robust and flexible electrocatalyst for CO_2 reduction with high efficiency and selectivity, Angew. Chem. Int. Ed. 56 (2017) 505–509, https://doi.org/10.1002/anie.201608279.

[46] X. Li, S. Xi, L. Sun, S. Dou, Z. Huang, T. Su, X. Wang, Isolated FeN_4 sites for efficient electrocatalytic CO_2 reduction, Adv. Sci. 7 (2020), 2001545, https://doi.org/10.1002/advs.202001545.

[47] F. Pan, B. Li, E. Sarnello, Y. Fei, X. Feng, Y. Gang, X. Xiang, L. Fang, T. Li, Y.H. Hu, G. Wang, Y. Li, Pore-edge tailoring of single-atom iron-nitrogen sites on graphene for enhanced CO_2 reduction, ACS Catal. 10 (2020) 10803–10811, https://doi.org/10.1021/acscatal.0c02499.